Terahertz plasmonics in ferroelectric-gated graphene

Dafei Jin, Anshuman Kumar, Kin Hung Fung, Jun Xu, and Nicholas X. Fang

Additional information on Appl. Phys. Lett.
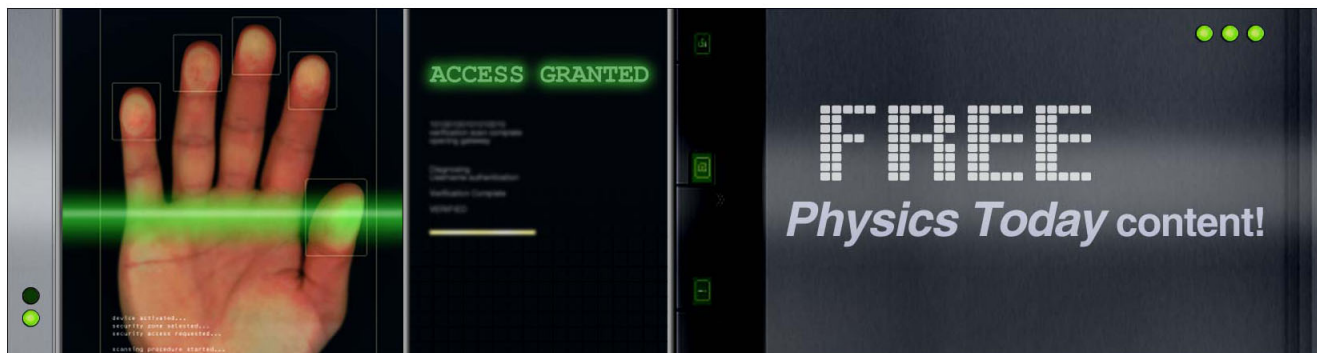
Terahertz plasmonics in ferroelectric-gated graphene

Dafei Jin,[1] Anshuman Kumar,[1] Kin Hung Fung,[1,2] Jun Xu,[1] and Nicholas X. Fang[1]

[1]*Department of Mechanical Engineering, Massachusetts Institute of Technology, Cambridge, Massachusetts 02139, USA*
[2]*Department of Applied Physics, The Hong Kong Polytechnic University, Hong Kong, China*

Inspired by recent advancement of ferroelectric-gated memories and transistors, we propose a design of ferroelectric-gated nanoplasmonic devices based on graphene sheets clamped in ferroelectric crystals. We show that the two-dimensional plasmons in graphene can strongly couple with the phonon-polaritons in ferroelectrics, leading to characteristic modal wavelength of the order of 100–200 nm at low temperature and low-THz frequencies albeit with an appreciable dissipation. By patterning the ferroelectrics into different domains, one can produce compact on-chip plasmonic waveguides, which exhibit negligible crosstalk even at 20 nm separation distance. Harnessing the memory effect of ferroelectrics, low-power operation can be achieved on these plasmonic waveguides. © *2013 AIP Publishing LLC*. [http://dx.doi.org/10.1063/1.4807762]

The emergence of graphene research in the recent years has triggered a significant interest in two-dimensional plasmonics.[1–6] The charge carriers in graphene exhibit perfect electron-hole symmetry and high mobility at low concentration.[7–11] The concentration (or the Fermi level) can be conveniently adjusted via chemical doping and electrostatic gating, which give rise to tunable plasmonic excitation in the terahertz frequency regime. In combination with its remarkable character of single-atom thickness and the ability of subwavelength light confinement, graphene has become a promising platform for the new-generation nanoplasmonic devices.[2–6] So far, the most widely studied graphene plasmonic structures are fabricated on silicon dioxide (SiO_2) substrates or suspended in air,[12,13] where the SiO_2 and air serve as the dielectric claddings for the creation of surface plasmon-polaritons (SPPs).[14] In contrast with conventional dielectrics, ferroelectrics such as lithium niobate ($LiNbO_3$) and lithium tantalate ($LiTaO_3$) bear giant permittivity and birefringence at terahertz frequencies.[15,16] This peculiarity is associated with the coexistence of terahertz phonon-polariton modes[17,18] and static macroscopic polarization.[19,20] It is thus of particular interest to investigate whether the unique properties of ferroelectrics can be integrated into nanoplasmonics,[20–22] and especially, display a strong coupling with graphene plasmonics in the same terahertz range.

In this paper, we propose a design of ferroelectric-gated graphene plasmonic devices operating at low-THz frequencies. Figure 1 illustrates the building blocks, while more complex structures can be made based on the same idea. This type of architecture has at least two appealing features that are not present in the common dielectric-graphene-dielectric architecture, and may bring fresh insight into the design of (classical or quantum) optical circuits. The first feature originates from the extremely large permittivity and comparatively high Q-value near the optical-phonon resonances of ferroelectrics at terahertz frequencies.[15] When the two-dimensional plasmons in graphene become coupled with the phonon-polaritons in ferroelectrics by exchanging photons across their interfaces, they form the so-called surface plasmon-phonon-polaritons (SPPPs) and lead to around

100 nm modal wavelength, even if the driving frequency remains at a few THz. These subwavelength modes are fundamentally supported by the atomic-level oscillations of ferroelectric ions and are limited by the dissipation through anharmonic phonon processes.[17,23,24] (By contrast, the typical modal wavelength would be ten times greater in SiO_2 cladding, owing to the much smaller permittivity in the same frequency range.[25]) The second feature lies in the large macroscopic polarization in ferroelectrics of the order of $10 \, \mu C \, cm^{-2}$, corresponding to a large surface bound-charge density of the order of $10^{14} \, cm^{-2}$.[18,19] The parallel- and antiparallel-poling configurations can induce drastically different charge-carrier densities on graphene, which effectively switch off and on the Fermi energy by about 1 eV. These features may be employed for constructing nanoplasmonic elements (waveguides, resonators, antennae, etc.) through the electrostatic gating by ferroelectrics.[20,26] Thanks to the memory effect of ferroelectrics, an intended design can sustain itself without a need of constant input bias, and can be conveniently refreshed at will, similar to the low-power operation in the ferroelectric random-access memories (FeRAM) and ferroelectric field-effect transistors (FeFETs).[19,27,28]

Let us first study the eigen-modes on an infinite ferroelectric-graphene-ferroelectric structure. Suppose the layered materials are stacked along the z-axis, and infinitely extended in the xy-plane, with the coordinate system indicated in Fig. 1. The graphene sheet is situated at $z = 0$ with a zero thickness yet a nonzero two-dimensional conductivity σ_g.[1,3,4] The two ferroelectric crystals occupy the semi-infinite regions $z < 0$ and $z > 0$, respectively. We assume the macroscopic polarizations of the ferroelectrics to be aligned with either $+z$ or $-z$ direction, so the optical axes of the crystals always coincide with the z-axis.[18] The static polarity mainly affects the electron density on graphene while has little impact on the optical properties in bulk crystals.[19,27,28] The eigen-solutions of the entire structure can be labeled by the frequency ω and the in-plane wavenumbers k_x and k_y across all the regions. Within each region, the electric field $\boldsymbol{E}$ and the magnetic field $\boldsymbol{H}$ are linear combinations of
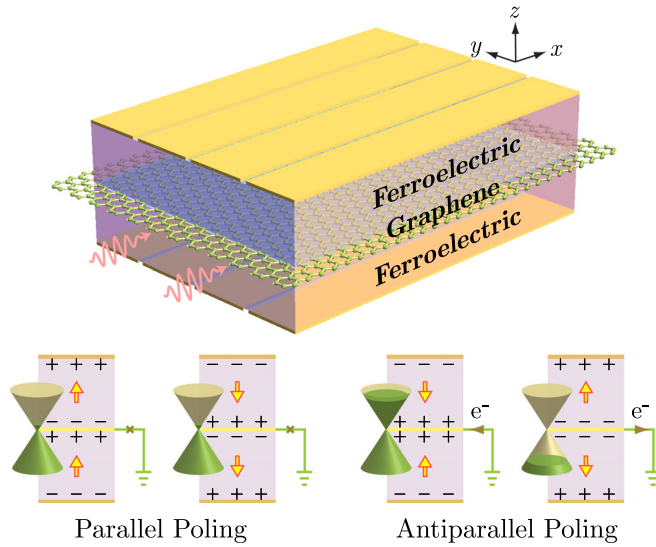
FIG. 1. Schematics of a ferroelectric-graphene-ferroelectric structure with parallel- and antiparallel-poling domains of the macroscopic polarization in the ferroelectrics. Parallel poling does not change the Fermi level of graphene from chemical doping, while antiparallel poling can induce an extra (positive or negative) electrostatic gating effectively.

plane waves containing an out-of-plane wavenumber k_z. For surface-wave solutions, k_z is mostly imaginary-valued like $k_z = i\kappa$. Due to anisotropy, we may define the ordinary and extraordinary two evanescent wavenumbers with respect to the optical z-axis, $\kappa_o^2 \equiv -k_z^2 = (k_x^2 + k_y^2) - (\omega^2/c^2)\epsilon_o$, $\kappa_e^2 \equiv -k_z^2 = (k_x^2 + k_y^2)\epsilon_o/\epsilon_e - (\omega^2/c^2)\epsilon_o$, respectively, where ϵ_o and ϵ_e are the ordinary and extraordinary permittivities of the ferroelectrics.[15,16] We shall eventually obtain the dispersion relation (in the cgs units),

$$2\frac{\epsilon_o}{\kappa_e} = \frac{4\pi\sigma_g}{i\omega}, \tag{1}$$

which is an anisotropic generalization to the dispersion relation in dielectric-graphene-dielectric structures.[1]

In graphene plasmonics, the Fermi energy E_F measured from the Dirac point usually ranges from about $\pm 0.05\,\text{eV}$ to $\pm 1.0\,\text{eV}$, equivalent to an electron or hole concentration n_c varying from $1.84 \times 10^{11}\,\text{cm}^{-2}$ to $7.35 \times 10^{13}\,\text{cm}^{-2}$ according to the relation $n_c = (|E_F|/\hbar v_F)^2/\pi$, where v_F is the Fermi velocity being about $1 \times 10^8\,\text{cm s}^{-1}$.[7–11,29] For the experiments below 10 THz, the simple Drude formula can quite accurately describe the graphene conductivity,[1–4] $\sigma_g = ie^2|E_F|/\pi\hbar^2(\omega + i\gamma_g)$, where γ_g is the relaxation rate. For an ultra-pure sample, the mobility limitation comes from the electron scatterings with the thermally excited acoustic phonons in graphene and the remote optical phonons from, e.g., SiO_2.[8–12,30] Referring to the existing literature for high-κ substrates,[30,31] we tentatively estimate the carrier mobility μ in our structure to be in the range of 1×10^4 to $8 \times 10^4\,\text{cm}^2\,\text{V}^{-1}\text{s}^{-1}$ at room temperature ($\sim 300\,\text{K}$), and 1×10^5 to $2 \times 10^5\,\text{cm}^2\,V^{-1}\,\text{s}^{-1}$ at low temperature ($\sim 100\,\text{K}$). The relaxation rate can be calculated from the mobility via $\gamma_g = ev_F^2/\mu|E_F|$,[10,11] where μ is assumed to be independent of n_c or E_F. Nevertheless, it is worthwhile to point out that the carrier mobility in graphene typically decreases with increasing carrier concentration and also decreases with

increasing dielectric constant of its surroundings, as shown in Refs. 8–10, 30, and 31. Direct measurement to our proposed structure is necessary.

For further studies, we choose $LiNbO_3$ as the ferroelectric material, which is especially convenient for low-THz experiments, because the extraordinarily polarized THz waves can be triggered by 800 nm femtosecond laser pulses via nonlinear optical response inside $LiNbO_3$.[15] According to the Raman scattering data,[18,32,33] $LiNbO_3$ has two fundamental transverse optical-phonon frequencies ω_{To} and ω_{Te}, corresponding to the ordinary and extraordinary waves, respectively. The main behaviors of the permittivities ϵ_o and ϵ_e in the 0.1–10 THz frequency range can be fitted by the Lorentz model,[15,17] $\epsilon_o(\omega) = \epsilon_o(\infty) + (\epsilon_o(0) - \epsilon_o(\infty))\omega_{To}^2/(\omega_{To}^2 - \omega^2 - i\gamma_o\omega)$, $\epsilon_e(\omega) = \epsilon_e(\infty) + (\epsilon_e(0) - \epsilon_e(\infty))\omega_{Te}^2/(\omega_{Te}^2 - \omega^2 - i\gamma_e\omega)$, where $\epsilon_o(\infty), \epsilon_o(0), \epsilon_e(\infty), \epsilon_e(0)$ are the high-frequency and low-frequency limits of ϵ_o and ϵ_e, γ_o and γ_e are the relaxation rates associated with anharmonic optical-phonon decaying. We adopt the following values for the dielectric properties, $\epsilon_o(\infty) = 19.5, \epsilon_o(0) = 41.5$, $\epsilon_e(\infty) = 10.0, \epsilon_e(0) = 26.0, \omega_{To} = 2\pi \times 4.6\,\text{THz}, \omega_{Te} = 2\pi \times 7.6\,\text{THz}$, and the following values for the dissipation strength, $\gamma_o = 0.51\,\text{THz}, \gamma_e = 0.84\,\text{THz}$, at room temperature ($\sim 300\,\text{K}$),[15] and $\gamma_o = 0.17\,\text{THz}, \gamma_e = 0.28\,\text{THz}$, at low temperature ($\sim 100\,\text{K}$). The phonon decaying at low temperature decreases to only about one thirds of the room-temperature strength.[32,33] ϵ_e and ϵ_o undergo near divergence and sign change around ω_{To} and ω_{Te}, signifying the high-Q resonant coupling between photons and optical phonons. They turn back to positive at the longitudinal optical-phonon frequencies $\omega_{Lo} = \omega_{To}\sqrt{\epsilon_o(0)/\epsilon_o(\infty)} = 2\pi \times 6.7\,\text{THz}$ and $\omega_{Le} = \omega_{Te}\sqrt{\epsilon_e(0)/\epsilon_e(\infty)} = 2\pi \times 12.3\,\text{THz}$ in this model.[15,17]

For plane waves, we set $k_y = 0$ without loss of generality, and explicitly derive k_x as

$$k_x^2 = \epsilon_e(\omega)\frac{\omega^2}{c^2} + \frac{\epsilon_o(\omega)\epsilon_e(\omega)}{(2e^2|E_F|/\hbar^2)^2}\omega^2\left(\omega + i\frac{ev_F^2}{\mu|E_F|}\right)^2. \tag{2}$$

The modal wavelength $\lambda = 2\pi/\text{Re}[k_x]$, the attenuation length $\xi = 1/\text{Im}[k_x]$, and the confining length $l = 1/\text{Re}[\kappa_e]$ can be defined accordingly. For a Fermi energy between 0.05 and 1.0 eV, and driving frequency in the range of 1–10 THz, the dispersion relation is primarily controlled by the second term of Eq. (2). The plasmon behavior is strongly affected by the optical-phonon resonances. So the combined excitations are SPPPs. Figure 2 shows the dispersion relation $\omega(\text{Re}[k_x])$ under different conditions. For each given E_F, the dispersion curves mainly stay in the three allowed-bands: $\omega < \omega_{To}$, $\omega_{Lo} < \omega < \omega_{Te}$, and $\omega > \omega_{Le}$, but weakly leak into the two forbidden-bands: $\omega_{To} < \omega < \omega_{Lo}$ and $\omega_{Te} < \omega < \omega_{Le}$. The finite-valued relaxation rates broaden the sharp peaks around the optical-phonon resonances. For a small E_F, the dispersion curves bend more considerably towards the optical-phonon lines and can give very large k_x at low frequencies; for a large E_F, the dispersion curves mostly attach to the THz light line (very close to the ω-axis and cannot be identified in the scale of Fig. 2). In reality, there exist other optical-phonon resonances higher than ω_{To} and ω_{Te},[32,33] which will make the curves in Fig. 2 more kinked than as shown. But we will
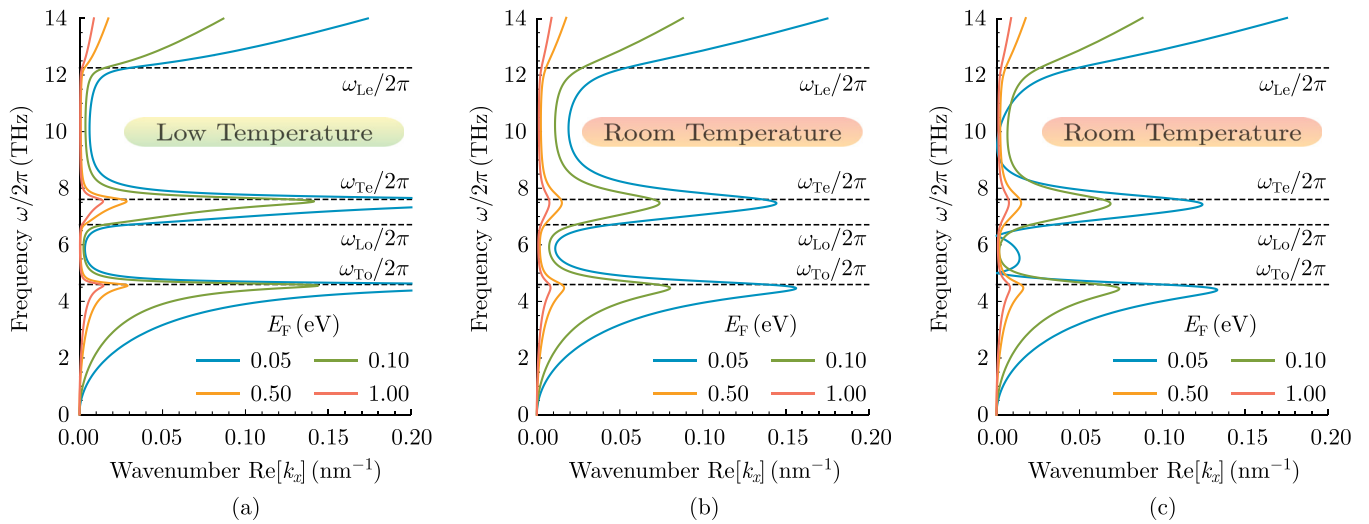
FIG. 2. Dispersion relations of surface plasmon-phonon-polaritons for different Fermi energies on a graphene sheet clamped in LiNbO$_3$ crystals in the low-temperature ($\sim$100 K) and room-temperature ($\sim$300 K) conditions. The carrier mobility is taken as (a) 2×10^5 cm^2 V^{-1}s^{-1}, (b) 8×10^4 cm^2 V^{-1}s^{-1}, and (c) 2×10^4 cm^2 V^{-1}s^{-1}, all assumed to be independent of the concentration (or Fermi energy).

only focus on the frequency region close to the fundamental optical-phonon resonance $\omega_{To} = 2\pi \times 4.6$ THz from below. In Table I, we list the calculated characteristic quantities at about 100 K. For sensitive THz-photon manipulation, a low temperature is helpful for suppressing the thermal noise or dissipation.[10,11,32,33] In Table I, one can see clearly the huge effective refractive index and ultra-short modal wavelength compared with the free-space wavelength of low-THz photons. Large dissipation occurs at frequencies above 4 THz; whereas below 4 THz, for $E_F \lesssim 0.1$ eV, the wavelength can indeed be squeezed to 100–200 nm while the confining length is only about 10–20 nm.

As an example, we now employ the large difference in the length scale of SPPPs under different Fermi energies to make subwavelength waveguides. LiNbO$_3$ is known to possess very large spontaneous polarization P_s. In a bulk crystal under zero electric field, $P_s \approx 70$ μC cm^{-2},[18,34] which is equivalent to a surface bound-charge density $n_s \approx 4.4 \times 10^{14}$ cm^{-2}. In a thin film of about 200 nm thick, $P_s \approx 5$ μC cm^{-2},[34] and the equivalent surface bound-charge

TABLE I. Calculated effective refractive index $\tilde{n}$, modal wavelength λ, attenuation length ξ, and confining length l of the surface plasmon-phonon-polaritons with several representative Fermi energies and frequencies at low temperature ($\sim$100 K).

E_F (eV)	$\omega/2\pi$ (THz)	$\tilde{n}$	λ (nm)	ξ (nm)	l (nm)
0.05	2.5	532+41i	225	467	27
	3.5	921+71i	93	192	10
	4.5	2807+1126i	24	9	1
0.10	2.5	266+12i	451	1594	53
	3.5	461+25i	186	545	19
	4.5	1412+538i	47	20	3
0.50	2.5	53+1.0i	2252	18 381	266
	3.5	92+3.3i	929	4102	96
	4.5	284+104i	235	102	13
1.00	2.5	27+0.4i	4504	43 933	532
	3.5	46+1.6i	1858	8757	192
	4.5	142+52i	469	206	26

density is $n_s \approx 3.1 \times 10^{13}$ cm^{-2}. For our studies, we take the 200 nm thickness for each slab of LiNbO$_3$. As shown in Fig. 1, for the parallel-poling configuration, the bound charges of opposite signs from the lower and upper slabs cancel each other, leaving an approximately zero-potential setting for the graphene sheet. Thus, the charge-carrier density on graphene is solely determined by chemical doping. But for the antiparallel-poling configuration, the bound charges of the same sign from the both slabs cause a net positive or negative potential on the graphene sheet. For the 200 nm thin film clamping, the induced charge-carrier density is $n_c \approx 2n_s = 6.2 \times 10^{13}$ cm^{-2}, which is equivalent to a nearly ± 1 eV electrostatic gating based on the preceding calculation. In the numerical simulation below, we assume a small $E_F = 0.05$ eV built in graphene from chemical doping, which is reserved between the parallel-poling domains, but shifted to $E_F \approx 0.05 \pm 1.0$ eV $\approx \pm 1.0$ eV between the antiparallel-poling domains due to the ferroelectric gating. The small difference in $|E_F|$ between the electron and hole cases is neglected as 0.05 eV $\ll$ 1.0 eV. The electron-hole symmetry in graphene plays an important role here.

We choose the frequency 3.5 THz for all our finite-difference time-domain (FDTD) simulations. The free-space photon wavelength is 85.7 μm. For the domain poling configuration shown in Fig. 3, a single $E_F = 0.05$ eV channel is produced in between two $E_F = 1.0$ eV barriers. As can be inferred from our previous discussion, a low-E_F channel is more "dielectric" in the sense that it carries less charges but hosts more photons, whereas a high-E_F channel is more "metallic" in the sense that it carries more charges but permits less photons. Thus, the deep subwavelength SPPP modes preferably flow in the middle channel with tiny penetration into the barriers on the two sides. The lower panel of Fig. 3 shows the real and imaginary parts of the effective refractive index $\tilde{n}$ changing with the channel width. The waveguide mode undergoes exponentially stronger attenuation and weaker subwavelength when the channel width goes down to below 100 nm, consistent with the 93 nm plane-wave modal wavelength at 3.5 THz in Table I.
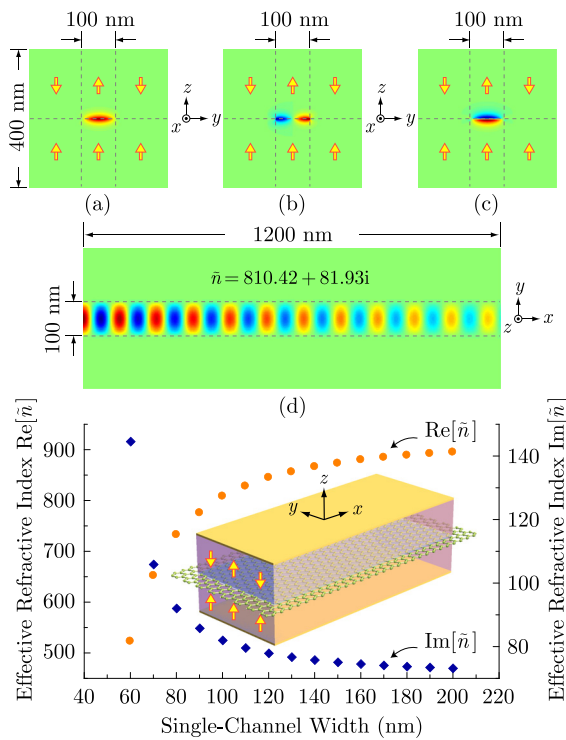
FIG. 3. Simulated effective refractive index of the fundamental waveguide mode in a parallel-poling channel between two antiparallel-poling barriers. Electric-field profiles for the case of 100 nm wide channel are plotted, in the *yz*-plane for (a) E_x, (b) E_y, (c) E_z, and in the *xy*-plane for (d) E_x. (The thick arrows indicate the domain orientations.)

We choose 100 nm to plot the profiles of each electric-field component in the upper panel of Fig. 3. For the effective refractive index $\tilde{n} = 810.42 + 81.93\mathrm{i}$ in this case, the modal wavelength $\lambda = 105.7$ nm, and the attenuation length $\xi = 166.4$ nm. In this regard, the dissipation is still appreciable even with relatively weak optical-phonon decaying and large carrier mobility at low temperature. We may increase the propagation distance by tuning to a lower driving frequency or higher Fermi energy (refer to Table I), but will unavoidably sacrifice some subwavelength features.

The exceptional confining quality of the prescribed ferroelectric-gated channel can be manifested by putting two such channels close to each other and see how the modes in the two channels become coupled by varying the separation distance.[13,35,36] We may define a dimensionless crosstalk number,

$$\mathcal{C} \equiv -10\log_{10}\left|\frac{\mathrm{Re}[\tilde{n}_\mathrm{a}] + \mathrm{Re}[\tilde{n}_\mathrm{s}]}{4(\mathrm{Re}[\tilde{n}_\mathrm{a}] - \mathrm{Re}[\tilde{n}_\mathrm{s}])}\right|, \qquad (3)$$

where $\tilde{n}_\mathrm{a}$ and $\tilde{n}_\mathrm{s}$ are the effective refractive indices of the antisymmetric and symmetric coupling modes, respectively. This crosstalk number estimates (in terms of dB) the number of modal wavelength needed, for an injected power initially in one channel to be transferred into the other and then be transferred back. In Fig. 4, we can see the simulated crosstalk number falling in the range of -30 to -55 dB. For the plotted pattern of even just 20 nm separation distance, $\mathcal{C} = -29.5$ dB, still far below zero. Although dissipation has come in at a much shorter distance before the waves really travel that far,[36] this number does show the extreme
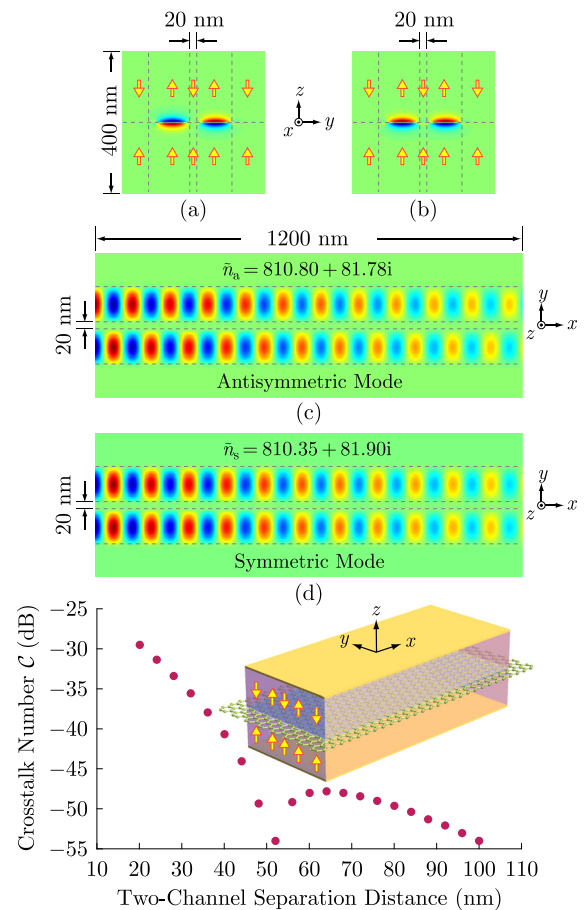

FIG. 4. Simulated crosstalk number based on the antisymmetric and symmetric waveguide modes in two 100 nm wide channels. Electric-field profiles for the case of 20 nm separation distance are plotted, in the *yz*-plane for (a) E_z of the antisymmetric mode, (b) E_z of the symmetric mode, and in the *xy*-plane for (c) E_x of the antisymmetric mode, (d) E_x of the symmetric mode. (The thick arrows indicate the domain orientations.)

confining quality in these ferroelectric-graphene waveguides compared with conventional dielectric and plasmonic waveguides. For example, silicon waveguides with the similar dimensions at the infrared frequencies have a crosstalk number of the order of -10 dB in accordance with our definition.[35] $\mathrm{Ba_{0.5}Sr_{0.5}TiO_3}$-metal inter-layer plasmonic waveguides at visible-light frequencies can have a crosstalk number of the order of -30 dB, but need a much larger separation distance.[21] There is a singular drop at about 50 nm on the calculated curve in the lower panel of Fig. 4. We find it to be due to a competition between the relative magnitudes of field components in this particular system. A large E_y favors a higher index for the symmetric mode, while a large E_x or E_z favors a higher index for the antisymmetric mode. The 50 nm separation distance between two 100 nm waveguides happens to be the turning point, where $\mathrm{Re}[\tilde{n}_\mathrm{a}] - \mathrm{Re}[\tilde{n}_\mathrm{s}] \simeq 0$.

[1]M. Jablan, H. Buljan, and M. Soljačić, Phys. Rev. B **80**, 245435 (2009).
[2]J. Long, B. Geng, J. Horng, C. Girit, M. Martin, Z. Hao, H. A. Bechtel, X. Liang, A. Zettl, Y. R. Shen, and F. Wang, Nat. Nanotechnol. **6**, 630 (2011).

[3]F. H. L. Koppens, D. E. Chang, and F. J. García de Abajo, Nano Lett. **11**, 3370 (2011).

[4]Q. Bao and K. P. Loh, ACS Nano **6**, 3677 (2012).

[5]P. Avouris and F. Xia, MRS Bull. **37**, 1225 (2012).

[6]T. Otsuji, S. A. B. Tombet, A. Satou, H. Fukidome, M. Suemitsu, E. Sano, V. Popov, M. Ryzhii, and V. Ryzhii, MRS Bull. **37**, 1235 (2012).

[7]A. K. Geim and K. S. Novoselov, Nature Mater. **6**, 183 (2007).

[8]K. I. Bolotin, K. J. Sikes, J. Hone, H. L. Stormer, and P. Kim, Phys. Rev. Lett. **101**, 096802 (2008).

[9]S. V. Morozov, K. S. Novoselov, M. I. Katsnelson, F. Schedin, D. C. Elias, J. A. Jaszczak, and A. K. Geim, Phys. Rev. Lett. **100**, 016602 (2008).

[10]N. M. R. Peres, Rev. Mod. Phys. **82**, 2673 (2010).

[11]S. Das Sarma, S. Adam, E. H. Hwang, and E. Rossi, Rev. Mod. Phys. **83**, 407 (2011).

[12]J. H. Chen, C. Jang, S. Xiao, M. Ishigami, and M. S. Fuhrer, Nat. Nanotechnol. **3**, 206 (2008).

[13]J. Christensen, A. Manjavacas, S. Thongrattanasiri, F. H. L. Koppens, and F. J. García de Abajo, ACS Nano **6**, 431 (2012).

[14]E. N. Economou, Phys. Rev. **182**, 539 (1969).

[15]T. Feurer, N. S. Stoyanov, D. W. Ward, J. C. Vaughan, E. R. Statz, and K. A. Nelson, Annu. Rev. Mater. Res. **37**, 317 (2007).

[16]Y. M. Sun, Z. L. Mao, B. H. Hou, G. Q. Liu, and L. Wang, Chin. Phys. Lett. **24**, 414 (2007).

[17]N. W. Ashcroft and N. D. Mermin, *Solid State Physics* (Thomson Brooks/Cole, Charlotte, 1976).

[18]V. Marek, "First-principles study of ferroelectric oxides," Ph.D. dissertation (Université de Liège, 2003).

[19]M. Dawber, K. M. Rabe, and J. F. Scott, Rev. Mod. Phys. **77**, 1083 (2005).

[20]M. Lilienblum, A. Ofan, A. Hoffmann, O. Gaathon, L. Vanamurthy, S. Bakhru, H. Bakhru, R. M. Osgood, Jr., and E. Soergel, Appl. Phys. Lett. **96**, 082902 (2010).

[21]S. W. Liu and M. Xiao, Appl. Phys. Lett. **88**, 143512 (2006).

[22]M. J. Dicken, L. A. Sweatlock, D. Pacifici, H. J. Lezec, K. Bhattacharya, and H. A. Atwater, Nano Lett. **8**, 4048 (2008).

[23]A. Harhira, L. Guilbert, P. Bourson, and H. Rinnert, Phys. Status Solidi C **4**, 926 (2007).

[24]V. H. Arakelian and N. M. Hovsepian, Phys. Status Solidi B **164**, 147 (1991).

[25]E. D. Palik, *Handbook of Optical Constants of Solids* (Academic Press, San Diego, 1997).

[26]D. Li and D. A. Bonnell, Annu. Rev. Mater. Res. **38**, 351 (2008).

[27]Y. Zheng, G.-X. Ni, C.-T. Toh, M.-G. Zeng, S.-T. Chen, K. Yao, and B. Ozyilmaz, Appl. Phys. Lett. **94**, 163505 (2009).

[28]E. B. Song, B. Lian, S. M. Kim, S. Lee, T.-K. Chung, M. Wang, C. Zeng, G. Xu, K. Wong, Y. Zhou, H. I. Rasool, D. H. Seo, H.-J. Chung, J. Heo, S. Seo, and K. L. Wang, Appl. Phys. Lett. **99**, 042109 (2011).

[29]T. Fang, A. Konar, H. Xing, and D. Jena, Appl. Phys. Lett. **91**, 092109 (2007).

[30]A. Konar, T. Fang, and D. Jena, Phys. Rev. B **82**, 115452 (2010).

[31]X. Hong, A. Posadas, K. Zou, C. H. Ahn, and J. Zhu, Phys. Rev. Lett. **102**, 136808 (2009).

[32]P. Capek, G. Stone, V. Dierolf, C. Althouse, and V. Gopolan, Phys. Status Solidi C **4**, 830 (2007).

[33]M. L. Hu, C. T. Chia, J. Y. Chang, W. S. Tse, and J. T. Yu, Mater. Chem. Phys. **78**, 358 (2003).

[34]V. Joshi, D. Roy, and M. L. Mecartney, Appl. Phys. Lett. **63**, 1331 (1993).

[35]C. Yeh and F. Shimabukuro, *The Essence of Dielectric Waveguides* (Springer, New York, 2008).

[36]G. Veronis and S. Fan, Opt. Express **16**, 2129 (2008).